
























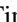
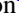







# TOI-677b: A Warm Jupiter ( $P = 11.2$ days) on an Eccentric Orbit Transiting a Late F-type Star

Andrés Jordán<sup>1,2</sup> , Rafael Brahm<sup>2,3,4</sup> , Néstor Espinoza<sup>5</sup> , Thomas Henning<sup>6</sup>, Matías I. Jones<sup>7</sup>, Diana Kossakowski<sup>6</sup>, Paula Sarkis<sup>6</sup> , Trifon Trifonov<sup>6</sup> , Felipe Rojas<sup>2,4</sup>, Pascal Torres<sup>2,4</sup>, Holger Drass<sup>3</sup>, Sangeetha Nandakumar<sup>8</sup>, Mauro Barbieri<sup>8</sup> , Allen Davis<sup>9</sup> , Songhu Wang<sup>9</sup>, Daniel Bayliss<sup>10</sup> , Luke Bouma<sup>11</sup> , Diana Dragomir<sup>12</sup> , Jason D. Eastman<sup>13</sup> , Tansu Daylan<sup>14,33</sup> , Natalia Guerrero<sup>14</sup> , Thomas Barclay<sup>15,16</sup> , Eric B. Ting<sup>17</sup>, Christopher E. Henze<sup>17</sup>, George Ricker<sup>14</sup>, Roland Vanderspek<sup>14</sup> , David W. Latham<sup>13</sup> , Sara Seager<sup>14,18,19</sup>, Joshua Winn<sup>11</sup> , Jon M. Jenkins<sup>17</sup> , Robert A. Wittenmyer<sup>20</sup> , Brendan P. Bowler<sup>21</sup> , Ian Crossfield<sup>22</sup>, Jonathan Horner<sup>20</sup> , Stephen R. Kane<sup>23</sup> , John F. Kielkopf<sup>24</sup> , Timothy D. Morton<sup>25</sup> , Peter Plavchan<sup>26</sup> , C. G. Tinney<sup>27</sup> , Brett Addison<sup>20</sup>, Matthew W. Mengel<sup>20</sup>, Jack Okumura<sup>20</sup>, Sahar Shahaf<sup>28</sup>, Tsevi Mazeh<sup>28</sup>, Markus Rabus<sup>29,30</sup> , Avi Shporer<sup>14</sup> , Carl Ziegler<sup>31</sup> , Andrew W. Mann<sup>32</sup> , and Rhodes Hart<sup>20</sup>

<sup>1</sup> Facultad de Ingeniería y Ciencias, Universidad Adolfo Ibáñez, Av. Diagonal las Torres 2640, Peñalolén, Santiago, Chile; [andres.jordan@uai.cl](mailto:andres.jordan@uai.cl)

<sup>2</sup> Millennium Institute for Astrophysics, Chile

<sup>3</sup> Center of Astro-Engineering UC, Pontificia Universidad Católica de Chile, Av. Vicuña Mackenna 4860, 7820436 Macul, Santiago, Chile

<sup>4</sup> Instituto de Astrofísica, Pontificia Universidad Católica de Chile, Av. Vicuña Mackenna 4860, Macul, Santiago, Chile

<sup>5</sup> Space Telescope Science Institute, 3700 San Martin Drive, Baltimore, MD 21218, USA

<sup>6</sup> Max-Planck-Institut für Astronomie, Königstuhl 17, Heidelberg D-69117, Germany

<sup>7</sup> European Southern Observatory, Alonso de Córdova 3107, Vitacura, Casilla 19001, Santiago, Chile

<sup>8</sup> INCT, Universidad de Atacama, calle Copayapu 485, Copiapó, Atacama, Chile

<sup>9</sup> Department of Astronomy, Yale University, New Haven, CT 06511, USA

<sup>10</sup> Department of Physics, University of Warwick, Coventry CV4 7AL, UK

<sup>11</sup> Department of Astrophysical Sciences, Princeton University, 4 Ivy Lane, Princeton, NJ 08540, USA

<sup>12</sup> Department of Physics and Astronomy, University of New Mexico, 1919 Lomas Blvd NE, Albuquerque, NM 87131, USA

<sup>13</sup> Harvard-Smithsonian Center for Astrophysics, 60 Garden Street, Cambridge, MA 02138, USA

<sup>14</sup> Department of Physics and Kavli Institute for Astrophysics and Space Research, Massachusetts Institute of Technology, Cambridge, MA 02139, USA

<sup>15</sup> NASA Goddard Space Flight Center, 8800 Greenbelt Road, Greenbelt, MD 20771, USA

<sup>16</sup> University of Maryland, Baltimore County, 1000 Hilltop Circle, Baltimore, MD 21250, USA

<sup>17</sup> NASA Ames Research Center, Moffett Field, CA, 94035, USA

<sup>18</sup> Department of Earth, Atmospheric and Planetary Sciences, Massachusetts Institute of Technology, Cambridge, MA 02139, USA

<sup>19</sup> Department of Aeronautics and Astronautics, MIT, 77 Massachusetts Avenue, Cambridge, MA 02139, USA

<sup>20</sup> University of Southern Queensland, Centre for Astrophysics, West Street, Toowoomba, QLD 4350, Australia

<sup>21</sup> Department of Astronomy, The University of Texas at Austin, TX 78712, USA

<sup>22</sup> Department of Physics, Massachusetts Institute of Technology, Cambridge, MA, USA

<sup>23</sup> Department of Earth and Planetary Sciences, University of California, Riverside, CA 92521, USA

<sup>24</sup> Department of Physics and Astronomy, University of Louisville, Louisville, KY 40292, USA

<sup>25</sup> Department of Astronomy, University of Florida, 211 Bryant Space Science Center, Gainesville, FL, 32611, USA

<sup>26</sup> Department of Physics and Astronomy, George Mason University, 4400 University Drive MS 3F3, Fairfax, VA 22030, USA

<sup>27</sup> Exoplanetary Science at UNSW, School of Physics, UNSW Sydney, NSW 2052, Australia

<sup>28</sup> School of Physics and Astronomy, Tel Aviv University, Tel Aviv 69978, Israel

<sup>29</sup> Las Cumbres Observatory Global Telescope Network, Santa Barbara, CA 93117, USA

<sup>30</sup> Department of Physics, University of California, Santa Barbara, CA 93106-9530, USA

<sup>31</sup> Dunlap Institute for Astronomy and Astrophysics, University of Toronto, 50 St. George Street, Toronto, Ontario M5S 3H4, Canada

<sup>32</sup> Department of Physics and Astronomy, The University of North Carolina at Chapel Hill, Chapel Hill, NC 27599-3255, USA

Received 2019 October 30; revised 2019 December 16; accepted 2019 December 19; published 2020 March 6

## Abstract

We report the discovery of TOI-677 b, first identified as a candidate in light curves obtained within Sectors 9 and 10 of the *Transiting Exoplanet Survey Satellite* (TESS) mission and confirmed with radial velocities. TOI-677 b has a mass of  $M_p = 1.236_{-0.067}^{+0.069} M_J$ , a radius of  $R_p = 1.170 \pm 0.03 R_J$ , and orbits its bright host star ( $V = 9.8$  mag) with an orbital period of  $11.23660 \pm 0.00011$  d, on an eccentric orbit with  $e = 0.435 \pm 0.024$ . The host star has a mass of  $M_* = 1.181 \pm 0.058 M_\odot$ , a radius of  $R_* = 1.28_{-0.03}^{+0.03} R_\odot$ , an age of  $2.92_{-0.73}^{+0.80}$  Gyr and solar metallicity, properties consistent with a main-sequence late-F star with  $T_{\text{eff}} = 6295 \pm 77$  K. We find evidence in the radial velocity measurements of a secondary long-term signal, which could be due to an outer companion. The TOI-677 b system is a well-suited target for Rossiter–McLaughlin observations that can constrain migration mechanisms of close-in giant planets.

*Unified Astronomy Thesaurus concepts:* Exoplanets (498); Extrasolar gas giants (509); Exoplanet astronomy (486); Transit photometry (1709); Radial velocity (1332); Planet hosting stars (1242)

*Supporting material:* machine-readable tables

<sup>33</sup> Kavli fellow.

## 1. Introduction

In the past two decades the population of known transiting exoplanets has grown at an accelerating pace. While the *Kepler* satellite (Borucki et al. 2010) dominates the overall number of discoveries, the particular class of close-in gas giants around nearby stars were until recently most efficiently discovered by wide-field photometric series (e.g., Bakos et al. 2004, 2013; Pollacco et al. 2006; Pepper et al. 2007; Talens et al. 2017). Due to the biases inherent to ground-based observatories, most of the discoveries of these surveys have periods of  $P \lesssim 10$  days. Systems of stations around the globe such as the HATSouth survey (Bakos et al. 2013) can in principle improve the efficiency of discovery for longer periods, but the number of systems with  $P > 10$  days uncovered by wide-field ground-based surveys is small, with the current record holder being HATS-17b with  $P \approx 16$  days (Brahm et al. 2016).

The population of close-orbiting gas giants has opened a number of questions about their physical structural and dynamical evolution, which are still topics of active research (Dawson & Johnson 2018). In particular, the nature of the migration history and the detailed mechanism of radius inflation for hot Jupiters needs further elucidation. In order to make further progress on those fronts the population of warm giants, loosely defined as systems with periods  $P \gtrsim 10$  days, is of importance. They are close enough to the star that they are likely to have undergone significant migration, but not as close that tidal effects can erase the potential imprints of that migration (Albrecht et al. 2012; Dawson 2014; Li & Winn 2016). In the same vein, they are far enough from their parent star that their radii have not been inflated by the mechanism that acts to bloat the radii of hotter giants (Kovács et al. 2010; Demory & Seager 2011; Miller & Fortney 2011). But while it is clear that these systems are very interesting, the population of known warm giants around nearby stars (allowing the most detailed characterization) is still very small. The launch of the Transiting Exoplanet Survey Satellite (*TESS*) mission (Ricker et al. 2015) is changing that. By scanning nearby stars around the whole sky the expectation is that hundreds of giant planets with  $P \gtrsim 10$  days will be uncovered (Sullivan et al. 2015; Barclay et al. 2018).

In this work we present the discovery originating from a *TESS* light curve of an eccentric warm giant planet with a period of  $P = 11.23660 \pm 0.00011$  days orbiting a bright late-F star. This is part of a systematic effort to characterize warm giants in the southern hemisphere uncovered with *TESS*, which has contributed to the discovery and mass measurement of three warm giants already (Brahm et al. 2019; Huber et al. 2019; Rodriguez et al. 2019). The paper is structured as follows. In Section 2 we describe the observational material used to perform a global modeling of the system, as described in Section 3. The results are then discussed in Section 4.

## 2. Observations

### 2.1. TESS

Between 2019 March 1 and 2019 April 22, the *TESS* mission observed TOI-677 (TIC 280206394, 2MASS J09362869-5027478, TYC 8176-02431-1, *WISE* J093628.65-502747.3) during the monitoring of Sectors 9 and 10, using camera 3 and CCDs 1 and 2, respectively. The *TESS* Science Processing Operations Center (SPOC; for an overview of the processing it carries out see Jenkins et al. 2016) Transiting Planet Search

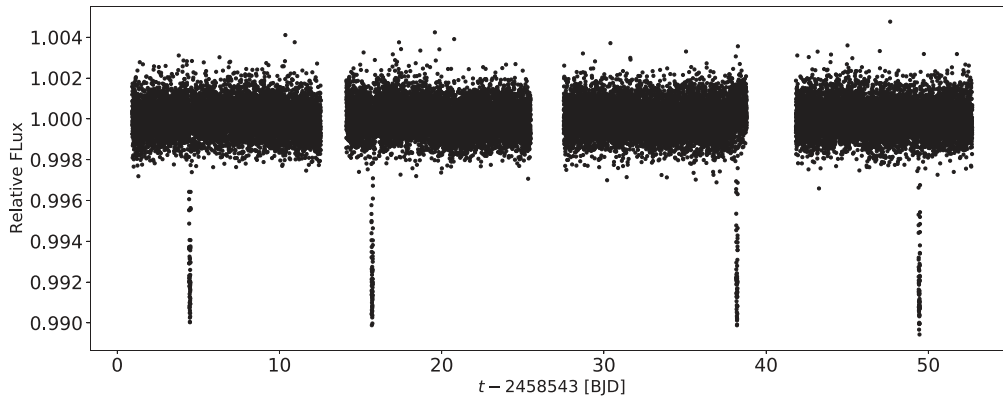
**Table 1**  
Stellar Properties of TOI-677

Parameter	Value	Reference
Names	TIC 280206394 2MASS J09362869-5027478 TYC 8176-02431-1 <i>WISE</i> J093628.65-502747.3	TIC 2MASS TYCHO <i>WISE</i>
R.A. (J2000)	15h32m17.84 s	
decl. (J2000)	-22d21m29.74 s	
$\mu_\alpha$ (mas yr <sup>-1</sup> )	-24.82 ± 0.05	<i>Gaia</i>
$\mu_\delta$ (mas yr <sup>-1</sup> )	42.42 ± 0.05	<i>Gaia</i>
$\pi$ (mas)	7.02 ± 0.03	<i>Gaia</i>
Spectral type	F8	
<i>TESS</i> (mag)	9.24 ± 0.018	TIC
<i>G</i> (mag)	9.661 ± 0.020	<i>Gaia</i>
<i>B<sub>p</sub></i> (mag)	9.968 ± 0.005	<i>Gaia</i>
<i>R<sub>p</sub></i> (mag)	9.229 ± 0.003	<i>Gaia</i>
<i>J</i> (mag)	8.722 ± 0.020	2MASS
<i>H</i> (mag)	8.470 ± 0.038	2MASS
<i>K<sub>s</sub></i> (mag)	8.429 ± 0.023	2MASS
<i>T</i> <sub>eff</sub> (K)	6295 ± 77	This work
log <i>g</i> (dex)	4.291 ± 0.025	This work
[Fe/H](dex)	0.00 ± 0.05	This work
<i>v</i> sin <i>i</i> (km s <sup>-1</sup> )	7.80 ± 0.19	This work
<i>M</i> <sub>*</sub> ( <i>M</i> <sub>⊙</sub> )	1.181 ± 0.058	This work
<i>R</i> <sub>*</sub> ( <i>R</i> <sub>⊙</sub> )	1.28 <sup>+0.03</sup> <sub>-0.03</sub>	This work
Age (Gyr)	2.92 <sup>+0.80</sup> <sub>-0.73</sub>	This work
$\rho_*$ (g cm <sup>-3</sup> )	0.80 <sup>+0.06</sup> <sub>-0.06</sub>	This work

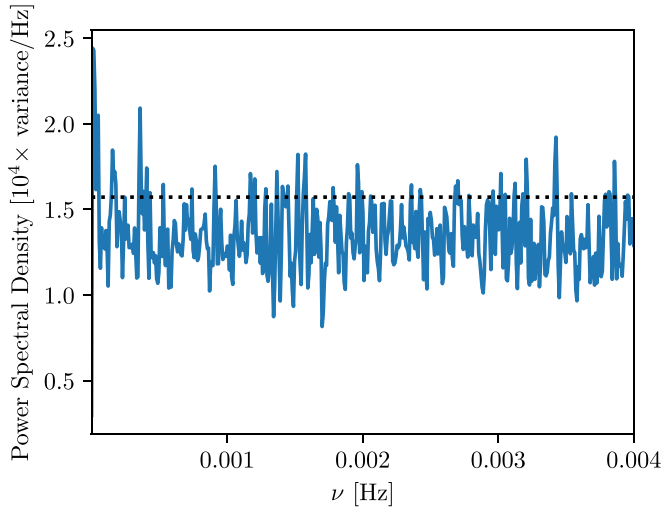
module detected the planetary signature in the Sector 9 processing run and in the Sectors 1–13 multi-sector search and triggered the data validation module (Twicken et al. 2018; Li et al. 2019) to analyze the transit-like feature in Sector 9 and combined the light curves of Sectors 9 and 10. All diagnostics tests performed as part of the data validation report, including the odd/even depth test, the signal-to-noise ratio (S/N), the impact parameter, the statistical bootstrap probability, the ghost diagnostic, and the difference image centroid offset from the TIC position and from the out-of-transit centroid, strongly favored the planetary hypothesis and resulted in the promotion of TOI-677 to the list of targets of interest.

The properties of TOI-677 as obtained from literature sources and derived in this work are detailed in Table 1. The target was observed in short (2 minutes) cadence, and we downloaded the pre-search data conditioning (PDC) simple aperture photometry (SAP) light curves from the Mikulski Archives for Space Telescopes. The PDC SAP light curves have systematic trends removed using co-trending basis vectors (Smith et al. 2012; Stumpe et al. 2014), and are produced by the *TESS* SPOC at the NASA Ames Research Center. We masked the regions of high scattered light as indicated in the data release notes for each of the sectors, augmenting the masked windows in a few cases where it was evident that there were some remaining trends that were insufficiently masked.<sup>34</sup> We did not mask data points with data quality flags, as we noticed that all of the second transit had been masked with a flag value of 2048 (stray light from Earth or the Moon in the camera field of view), but inspection

<sup>34</sup> In detail, in the first and second orbits of Sector 10 we excluded up to cadence numbers 247,000 and 257,300, respectively, instead of the values 246,576 and 256,215 indicated in the data release notes for Sector 10.



**Figure 1.** Two-minute cadence *TESS* light curve. These are the PDC SAP measurements produced by the SPOC pipeline. Four transits are clearly seen in the *TESS* photometry, with the middle transit falling within a gap.



**Figure 2.** Power spectral density of the out-of-transit *TESS* light curve. The dashed line marks the expected value of the power spectral density, estimated as  $\langle \sigma_i^2 \rangle / (\nu_u - \nu_l)$ , where  $\langle \sigma_i^2 \rangle$  is the average measurement variance of the *TESS* photometry,  $\nu_l = 0$ , and  $\nu_u \approx 0.004$  Hz is the Nyquist frequency for the short cadence sampling.

of the masked portions revealed no anomalous signs on the light curve.

The *TESS* light curve is shown in Figure 1, where four transits are clearly seen. The out-of-transit light curve is remarkably flat. We estimated the power spectral density of the out-of-transit light curve of TOI-677 using the method of Welch (1967) as implemented in the `scipy.signal` Python module and found it to be featureless and at precisely the level expected given the reported photometric uncertainties of the magnitude measurements (see Figure 2). We conclude from this exercise that there is no need for any deterministic or stochastic component beyond the white noise implied by the photometric uncertainties in the modeling of the out-of-transit light curve. Because of this we only fit for regions of  $\approx 1$  day around each transit, removing the median value calculated in the out-of-transit portion for each transit. The *TESS* data used for the analysis is presented in Table 2.

## 2.2. Spectroscopy

We followed up TOI-677 with several spectrographs in order to confirm the *TESS* transiting planet candidate and to measure its mass. In what follows we describe the observations obtained

**Table 2**  
Relative Photometry for TOI-677<sup>a</sup>

BJD (2,400,000+)	$f$ (ppt)	$\sigma_f$ (ppt)	Instrument
58547.001330	-0.199	0.789	<i>TESS</i>
58547.002719	1.058	0.790	<i>TESS</i>
58547.004108	0.339	0.789	<i>TESS</i>
58547.005496	-1.082	0.790	<i>TESS</i>
58547.006885	0.377	0.790	<i>TESS</i>
58547.008274	1.051	0.790	<i>TESS</i>
58547.009663	0.314	0.789	<i>TESS</i>
58547.011052	1.058	0.790	<i>TESS</i>
58547.012441	-0.483	0.790	<i>TESS</i>
58547.013830	0.617	0.789	<i>TESS</i>
58547.015219	-0.675	0.790	<i>TESS</i>
58547.016608	-0.039	0.789	<i>TESS</i>
58547.017997	0.166	0.790	<i>TESS</i>
58547.019386	0.393	0.788	<i>TESS</i>
58547.020774	-0.916	0.790	<i>TESS</i>
58547.022163	-1.167	0.789	<i>TESS</i>
58547.023552	2.311	0.790	<i>TESS</i>
58547.024941	1.251	0.790	<i>TESS</i>
58547.026330	0.043	0.789	<i>TESS</i>
58547.027719	-0.603	0.790	<i>TESS</i>

**Note.**

<sup>a</sup> Table 2 is published in its entirety in machine readable format. A portion is shown here for guidance regarding its form and content.

(This table is available in its entirety in machine-readable form.)

by each spectrograph we used. The derived radial velocities, and bisector span measurements when available, are reported in Table 4.

### 2.2.1. FEROS

TOI-677 was monitored with The Fiber-fed Extended Range Optical Spectrograph (FEROS;  $R \approx 48,000$ , Kaufer et al. 1999) mounted at the MPG 2.2 m telescope at La Silla Observatory between 2019 May and July, where 26 spectra were obtained. Observations were performed in simultaneous calibration mode, with the secondary fiber observing a thorium–argon (ThAr) lamp to trace the instrumental variations produced by changes in the environment during the science exposures. The adopted exposure times were of 300 and 400 s, which translated into an S/N ranging between 40 and 150 per resolution element. The FEROS data were processed with the

CERES pipeline (Brahm et al. 2017a), which delivers the radial velocities corrected by the instrumental drift variations and the by the Earth’s motion. These radial velocities were obtained with the cross-correlation technique, where a G2-type binary mask was used as a template. From this cross-correlation peak CERES also computes the bisector span measurements, and delivers a rough estimate of the stellar parameters by comparing the continuum normalized spectrum with a grid of synthetic ones.

### 2.2.2. Coralie

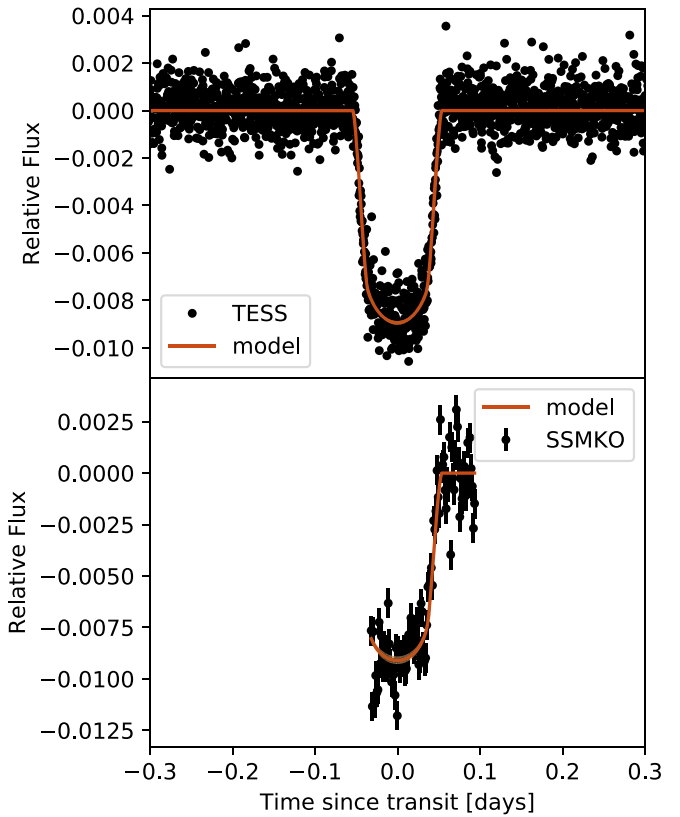
We monitored TOI-677 with the Coralie spectrograph ( $R \approx 60,000$ ; Mayor et al. 2003) mounted on the Swiss-Euler 1.2 m telescope in six different epochs. These observations were also performed with the simultaneous calibration technique, but in this case the secondary fiber is illuminated by a Fabry–Perot etalon. We adopted an exposure time of 300 s, which produced spectra having a typical S/N of 30 per resolution element. Coralie data were also processed with the CERES pipeline for obtaining the radial velocities.

### 2.2.3. CHIRON

We collected a total of 11 spectra of TOI-677 using the CHIRON high-resolution spectrograph (Tokovinin et al. 2013) between 2019 May 17 and June 19. The exposure time was between 750 and 1200 s, leading to an S/N per pixel between  $\approx 20$  and 35. CHIRON is mounted on the Small and Moderate Aperture Research Telescope System (SMARTS) 1.5 m telescope at the Cerro Tololo Inter-American observatory in Chile, and is fed by an octagonal multi-mode optical fiber. For these observations we used the image slicer, which delivers relatively high throughput and high spectral resolution ( $R \approx 80,000$ ). The radial velocities were computed from the cross-correlation function between the individual spectra and a high-resolution template of the star, which is built by stacking all individual observations of this star. Since CHIRON is not equipped with a simultaneous calibration, we observed the spectrum of a ThAr lamp before the science observations, to correct for the instrumental drift. Using this method we have measured a long-term radial velocity stability of  $< 10 \text{ m s}^{-1}$  on bright targets ( $t_{\text{exp}} < 60 \text{ s}$ ) and  $< 15 \text{ m s}^{-1}$  for fainter objects ( $t_{\text{exp}} < 1800 \text{ s}$ ). For more details of the method see Wang et al. (2019) and Jones et al. (2019).

### 2.2.4. NRES

Las Cumbres Observatory’s Network of Robotic Echelle Spectrographs (NRES; Siverd et al. 2018) is a global array of echelle spectrographs mounted on 1 m telescopes, with a resolving power of  $\approx 53,000$ . TOI-677 was observed at 12 epochs with the NRES node located at the Cerro Tololo Inter-American Observatory. At each observing epoch, three consecutive 1200 s exposures were obtained, with an individual S/N  $\gtrsim 40$ . The velocity of each exposure was derived via cross-correlation with a PHOENIX template (Husser et al. 2013) with  $T_{\text{eff}} = 5800 \text{ K}$ ,  $\log g = 3.5$ ,  $[\text{Fe}/\text{H}] = -0.5$ , and  $v \sin i = 7 \text{ km/s}$ . Systematic drifts were corrected per order (e.g., Engel et al. 2017) and the radial velocity of each epoch was then taken as the mean of the three exposures.



**Figure 3.** Photometric data with the trend subtracted as a function of phase for the two photometric instruments used in this work (TESS, SSMKO). The orange line shows the posterior transit model.

### 2.2.5. Minerva-Australis

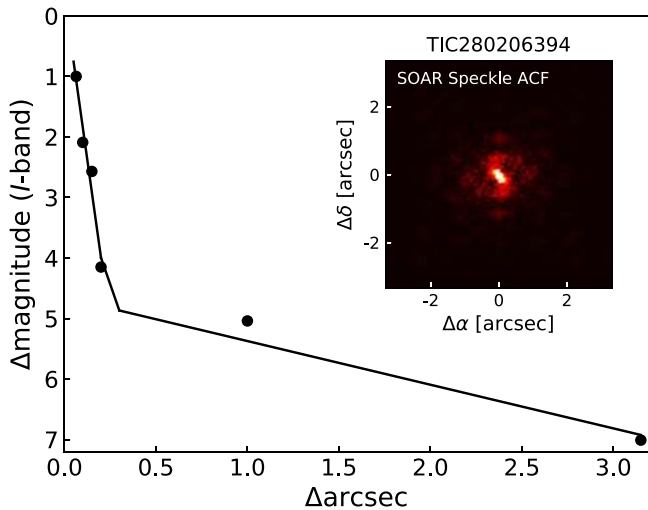
We obtained 17 observations on nine separate nights with the Minerva-Australis telescope array (Addison et al. 2019) at Mount Kent Observatory in Queensland, Australia. All of the telescopes in the Minerva-Australis array simultaneously feed a single Kiwispec R4-100 high-resolution ( $R \approx 80,000$ ) spectrograph with a wavelength coverage from 500 to 630 nm over 26 echelle orders. We derived radial velocities for each telescope using the least-squares analysis of Anglada-Escudé & Butler (2012) and corrected for spectrograph drifts with simultaneous ThAr arc lamp observations. TOI-677 was observed with telescopes 3, 4, and 5 of the array, and the derived radial velocities are reported under the instrument labels Minerva\_T3, Minerva\_T4, and Minerva\_T5 in Table 4.

## 2.3. Ground-based Photometry

### 2.3.1. Shared Skies Telescope at Mt. Kent Observatory (SSMKO)

TOI-677 was observed on the night of UTC 2019-05-09 with the University of Louisville’s Shared Skies MKO-CDK700 (SSMKO) telescope at Mt. Kent Observatory of the University of Southern Queensland, Australia. The telescope is a 0.7 m corrected Dall-Kirkham with a Nasmyth focus manufactured by Planewave. Images with an exposure time of 64 s were taken through a Sloan  $i'$  filter using an Apogee U16 CCD camera with a Kodak KAF-16801E sensor. A sequence of 92 images were acquired over 180 minutes. The light curve, which is shown in Figure 3, displays a clear egress. No significant activity or modulation other than the transit itself was apparent in the light curve, which shows residuals of 0.85 ppt at the





**Figure 4.** *I*-band autocorrelation function from Speckle using SOAR. The  $5\sigma$  contrast curve for TOI-677 is shown by the black points. The black solid line is the linear fit to the data for separations  $<0.2''$  and  $>0.2''$ . The autocorrelation function is shown within the contrast curve plot.

observational cadence. The SSMKO data used for the analysis is presented in Table 2.

#### 2.4. Gaia DR2

Observations of TOI-677 by *Gaia* were reported in DR2 (Gaia Collaboration et al. 2016, 2018). From *Gaia* DR2, TOI-677 has a parallax of  $7.02 \pm 0.03$  mas, an effective temperature of  $T_{\text{eff}} = 5895^{+105}_{-200}$  K, and a radius of  $R_* = 1.37^{+0.1}_{-0.05} R_\odot$ . The parallax obtained from *Gaia* was used to determine the stellar physical parameters of TOI-677 as described in Section 3.1. In our analysis we corrected the *Gaia* DR2 parallax for the systematic offset of  $-82 \mu\text{as}$  reported in Stassun & Torres (2018).

#### 2.5. High Spatial Resolution Imaging

The relatively large angle subtended by the *TESS* pixels, approximately  $21''$  on a side, leaves it susceptible to photometric contamination from nearby stars, including additional wide stellar companions. We searched for nearby sources to TIC 280206394 with the Southern Astrophysical Research (SOAR) telescope speckle imaging (Tokovinin 2018) on 2019 May 18 UT, observing through a similar visible bandpass as *TESS*. More details of these observations are available in Ziegler et al. (2020). We detected no nearby sources within  $3''$  of TIC 280206394. The  $5\sigma$  detection sensitivity and the speckle autocorrelation function from the SOAR observation are plotted in Figure 4.

The radial velocity variations measured on TOI-677 phase with the transit signal. This fact, combined with the lack of nearby companions, the lack of correlation of the bisector span measurements with orbital phase, and the tests carried out as part of the SPOC data validation report show that the transit is not caused by a blended stellar eclipsing binary.

### 3. Analysis

#### 3.1. Stellar Parameters

In order to characterize the star, we follow the same procedure presented in Brahm et al. (2019). First, we compute the stellar atmospheric parameters using the co-added FEROS spectra through the ZASPE code (Brahm et al. 2017b). ZASPE

estimates  $T_{\text{eff}}$ ,  $\log g$ ,  $[\text{Fe}/\text{H}]$ , and  $v \sin i$ , by comparing an observed spectrum with a grid of synthetic models generated with the ATLAS9 atmospheres (Castelli & Kurucz 2004).

Then, we estimate the physical parameters of the host star using the publicly available broadband photometry of *Gaia* ( $G$ ,  $B_p$ ,  $R_p$ ) and Two Micron All Sky Survey (2MASS) ( $J$ ,  $H$ ,  $K_s$ ), which is compared to the synthetic magnitudes provided by the Padova-Trieste Stellar Evolution Code (PARSEC) stellar evolutionary models using the distance to the star from the *Gaia* DR2 parallax. For a given stellar mass, age, and metallicity, the PARSEC models can deliver a set of synthetic absolute magnitudes and other stellar properties (e.g., stellar luminosity, effective temperature, stellar radius).

We determine the posterior distributions for  $M_*$ , age, and  $A_V$ , via a Markov Chain Monte Carlo (MCMC) code using the emcee package (Foreman-Mackey et al. 2013), where we fix the metallicity of the PARSEC models to that obtained with ZASPE, and we apply the Cardelli et al. (1989) extinction laws to the synthetic magnitudes.

This procedure provides a more precise estimation of  $\log g$  than the one obtained from the spectroscopic analysis. For this reason we iterate the procedure where we fix the  $\log g$  value when running ZASPE to the value obtained from the PARSEC models. The resulting values are  $T_{\text{eff}} = 6295 \pm 77$  K,  $[\text{Fe}/\text{H}] = 0.00 \pm 0.05$  dex,  $\log g = 4.291 \pm 0.025$ ,  $v \sin i = 7.80 \pm 0.19$  km s $^{-1}$ ,  $A_V = 0.226^{+0.056}_{-0.058}$  mag, age =  $2.92^{+0.80}_{-0.73}$  Gyr,  $L_* = 2.33 \pm 0.11 L_\odot$ ,  $M_* = 1.170 \pm 0.06 M_\odot$ , and  $R_* = 1.282 \pm 0.03 R_\odot$ . The values and uncertainties of  $M_*$  and  $R_*$  are used to define priors for them in the global analysis described in the next section.

#### 3.2. Global Modeling

We performed joint modeling of the radial velocity and photometric data using the exoplanet toolkit (Foreman-Mackey et al. 2019). The radial velocities used are given in Table 4 and the photometric data are given in Table 2. We denote the *TESS* photometric time series by  $\{y_T(t_i)\}_{i=1}^{n_T}$ , the SSMKO one by  $\{y_S(t_i)\}_{i=1}^{n_S}$ , and the radial velocity measurements (with their mean values removed) by  $\{y_F(t_i)\}_{i=1}^{n_F}$ ,  $\{y_C(t_i)\}_{i=1}^{n_C}$ ,  $\{y_Y(t_i)\}_{i=1}^{n_Y}$ ,  $\{y_N(t_i)\}_{i=1}^{n_N}$ , and  $\{y_{M(i)}(t_i)\}_{i=1}^{n_{M(i)}}$  for FEROS, Coralie, CHIRON, NRES, and Minerva-Australis respectively. In the case of Minerva,  $M(i)$  is a function that returns the telescope used at observation  $t_i$  (recall the Minerva observations include three different telescopes). The observational uncertainties are denoted by  $\sigma_*(t_i)$ , where  $*$  can take the value of any of the instrument labels. As shown in Section 2.1, the *TESS* light curve shows no evidence of additional structure beyond white noise. The *TESS* photometric time series is therefore modeled as

$$y_T(t_i) = \mathcal{T}(t_i; \mathbf{p}) + N(0, \sigma_{T,i}^2), \quad (1)$$

where  $N(0, \sigma^2)$  denotes a normal distribution of mean 0 and variance  $\sigma^2$ ,  $\mathcal{T}(t_i; \mathbf{p})$  is the transit model, and  $\mathbf{p}$  is the vector of model parameters. Explicitly,

$$\mathbf{p} = (R_p, \ln(M_p), b, P, t_0, e, \omega, R_*, M_*, u_1, u_2), \quad (2)$$

where  $R_p$  is the planetary radius,  $M_p$  is the planetary mass,  $b$  is the impact parameter,  $P$  is the period,  $t_0$  is the reference time of mid-transit,  $e$  is the eccentricity,  $\omega$  is the angle of periastron,  $R_*$  and  $M_*$  the stellar radius and mass, and  $u_1$  and  $u_2$  are the limb-darkening law coefficients, which we describe using a quadratic

law. The parameters  $R_p$  and  $b$  are derived from the parameters  $r_1$  and  $r_2$  defined in Espinoza (2018) to allow efficient sampling of physically possible combinations of  $b$  and  $R_p/R_*$ , so that from the sampled parameters  $r_1$ ,  $r_2$ , and  $R_*$  we determine  $b = b(r_1, r_2)$  and  $R_p = R_p(r_1, r_2, R_*)$ .

The SSMKO photometric time series is modeled as

$$\begin{aligned} y_S(t_i) &= \mathcal{T}(t_i; \mathbf{p}_u) + N(0, \sigma_{S,i}^2 + \eta_S^2) \\ &+ b_0 + b_1(t_i - t_0) \\ &\equiv \phi_S(t_i) + N(0, \sigma_{S,i}^2), \end{aligned} \quad (3)$$

where the  $\{b_i\}$  coefficients account for up to a linear systematic trend in the photometry,  $\sigma_{S,i}^2$  are the reported photometric uncertainties, and  $\eta_S$  is an additional photometric variance parameter. The parameter vector is the same as that for *TESS*, but the limb-darkening coefficients are fixed to the values  $(u_1, u_2) = (0.2489, 0.305)$ . These values were calculated using the ATLAS atmospheric models and the Sloan *i'* band using the limb-darkening coefficient calculator (Espinoza & Jordán 2015), and in particular using the methodology of sampling the limb-darkening profile in 100 points as described in Espinoza & Jordán (2015). We chose to fix the limb-darkening coefficients given that the SSMKO light curve covers only the egress. The radial velocity times series are modeled as

$$\begin{aligned} y_*(t_i) &= \mathcal{O}(t_i; \mathbf{q}) + N(0, \sigma_{*,i}^2 + \eta_*^2) + \gamma_* \\ &a_0 + a_1(t - t_0) \\ &\equiv r_*(t_i) + N(0, \sigma_{*,i}^2 + \eta_*^2) \end{aligned} \quad (4)$$

where  $\mathcal{O}$  represents the Keplerian radial velocity curve and the parameter vector of the model; a subset of  $\mathbf{p}$ , is  $\mathbf{q} = (P, \ln(M_p), t_0, e, \omega, M_*)$ . The wild card  $*$  in Equation (4) can take the values *F*, *C*,  $\chi$ , *N*, *M* for FEROS, Coralie, CHIRON, NRES, and Minerva respectively, and  $\eta_*^2$  is a white noise jitter term to account for additional variance not accounted for in the reported observational variances  $\sigma_{*,i}^2$ . The parameters  $\{a_i\}$  account for up to a linear systematic trend in the radial velocities. We set priors for  $\eta_*^2$  by first running a model without jitter terms, and determining for each instrument how much extra variance was present around the posterior model over that predicted by the observational uncertainties. We note that for NRES we found no need for a jitter term and thus we set  $\eta_N \equiv 0$ . The log-likelihood  $l$  is given by

$$\begin{aligned} -2l(\mathbf{p}) &= \sum_{i=1}^{n_r} \sigma_{T,i}^{-2} (y_{T,i} - \mathcal{T}_{T,i})^2 \\ &+ \sum_{i=1}^{n_s} (\sigma_{S,i}^2 + \eta_S^2)^{-2} (y_{S,i} - \phi_{S,i})^2 + \ln(\sigma_{S,i}^2 + \eta_S^2) \\ &+ \sum_{i=1}^{n_F} (\sigma_{F,i}^2 + \eta_F^2)^{-2} (y_{F,i} - r_{F,i})^2 + \ln(\sigma_{F,i}^2 + \eta_F^2) \\ &+ \sum_{i=1}^{n_C} (\sigma_{C,i}^2 + \eta_C^2)^{-2} (y_{C,i} - r_{C,i})^2 + \ln(\sigma_{C,i}^2 + \eta_C^2) \\ &+ \sum_{i=1}^{n_\chi} (\sigma_{\chi,i}^2 + \eta_\chi^2)^{-2} (y_{\chi,i} - r_{\chi,i})^2 + \ln(\sigma_{\chi,i}^2 + \eta_\chi^2) \\ &+ \sum_{i=0}^{n_M} (\sigma_{M(i),i}^2 + \eta_M^2)^{-2} \\ &\times (y_{M,i} - r_{M(i),i})^2 + \ln(\sigma_{M(i),i}^2 + \eta_M^2) \\ &+ \sum_{i=1}^{n_N} \sigma_{N,i}^{-2} (y_{N,i} - r_{N,i})^2. \end{aligned} \quad (5)$$

Posteriors were sampled using an MCMC algorithm, specifically the No U-Turn Sampler (NUTS; Hoffman & Gelman 2011) as

**Table 3**  
Prior and Posterior Parameters of the Global Fit

Parameter	Prior	Value
$P$ (days)	$N(11.27, 0.7^2)$	$11.23660 \pm 0.00011$
$T_0$ (BJD)	$N(2458547.4743, 0.0012^2)$	$2458547.47448^{+0.00028}_{-0.00029}$
$\ln(M_p/M_\oplus)$	$N(\ln(500), 0.3^2)$	$5.973^{+0.054}_{-0.056}$
$R_*$ ( $R_\odot$ )	$N(1.282, 0.03^2)$	$1.28^{+0.03}_{-0.03}$
$M_*$ ( $M_\odot$ )	$N(1.17, 0.06^2)$	$1.181 \pm 0.058$
$r1^a$	$U(0,1)$	$0.0942^{+0.0010}_{-0.0012}$
$r2^a$	$U(0,1)$	$0.723^{+0.018}_{-0.024}$
$u_1^{\text{TESS}}$	$U(0, 1)$	$0.50^{+0.19}_{-0.27}$
$u_2^{\text{TESS}}$	$U(0,1)$	$-0.06^{+0.33}_{-0.23}$
$e$	$N_b(0.4, 0.1; 0, 1)$	$0.435 \pm 0.024$
$\omega$ (rad)	$U(-\pi, \pi)$	$1.230^{+0.063}_{-0.063}$
$\gamma_{\text{FEROS}}$ ( $\text{m s}^{-1}$ )	$N(-40, 20^2)$	$-42.8^{+8.8}_{-8.6}$
$\gamma_{\text{Coralie}}$ ( $\text{m s}^{-1}$ )	$N(-20, 20^2)$	$-26.9^{+14.7}_{-15.4}$
$\gamma_{\text{CHIRON}}$ ( $\text{m s}^{-1}$ )	$N(-20, 20^2)$	$-20.9^{+10.7}_{-10.6}$
$\gamma_{\text{NRES}}$ ( $\text{m s}^{-1}$ )	$N(-20, 20^2)$	$-28.5^{+11.4}_{-11.4}$
$\gamma_{\text{Minerva}_{\text{T3}}}$ ( $\text{m s}^{-1}$ )	$N(0, 20^2)$	$4.2^{+10.1}_{-10.2}$
$\gamma_{\text{Minerva}_{\text{T4}}}$ ( $\text{m s}^{-1}$ )	$N(-20, 20^2)$	$-32.2^{+10.6}_{-10.5}$
$\gamma_{\text{Minerva}_{\text{T5}}}$ ( $\text{m s}^{-1}$ )	$N(0, 20^2)$	$20.9^{+12.7}_{-12.9}$
$\eta_{\text{FEROS}}$ ( $\text{m s}^{-1}$ )	$N_b(13, 5^2; 0, \infty)$	$13.5^{+3.3}_{-3.1}$
$\eta_{\text{Coralie}}$ ( $\text{m s}^{-1}$ )	$N_b(22, 10^2; 0, \infty)$	$45.1^{+12.4}_{-11.4}$
$\eta_{\text{CHIRON}}$ ( $\text{m s}^{-1}$ )	$N_b(45, 15^2; 0, \infty)$	$21.7^{+8.0}_{-7.6}$
$\eta_{\text{Minerva}}$ ( $\text{m s}^{-1}$ )	$N_b(30, 12^2; 0, \infty)$	$33.0^{+4.5}_{-3.8}$
$\eta_S$	$N_b(0.001, 0.0003^2; 0, \infty)$	$0.00114^{+0.00011}_{-0.00010}$
$a_0$ ( $\text{m s}^{-1}$ )	$N(0, 20^2)$	$-6.4^{+8.1}_{-8.2}$
$a_1$ ( $\text{m s}^{-1} \text{ day}^{-1}$ )	$N(0.7, 0.5^2)$	$1.58 \pm 0.19$
$b_0$	$N(0, 0.1^2)$	$-0.00197^{+0.00033}_{-0.00032}$
$b_1$ ( $\text{day}^{-1}$ )	$N(0, 0.01^2)$	$0.0204^{+0.0039}_{-0.0040}$
$b$		$0.723^{+0.018}_{-0.024}$
$i$ (deg)		$87.63^{+0.11}_{-0.1}$
$R_p/R_*$		$0.0942^{+0.0010}_{-0.0012}$
$R_p(R_j)$		$1.170 \pm 0.03$
$M_p(M_j)$		$1.236^{+0.069}_{-0.067}$
$a$ (au)		$0.1038^{+0.0017}_{-0.0017}$
$T_{\text{eq}}(\text{K})^b$		$1252 \pm 21$
$D(\text{days})^c$		$0.1074^{+0.0010}_{-0.0007}$

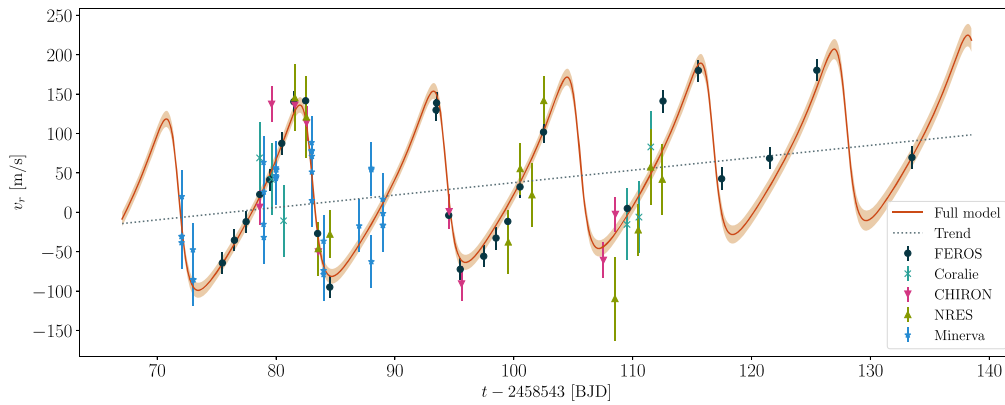
**Notes.** Derived parameters, which are deterministic functions of the parameters fitted for, are presented in the bottom part of the table. For the priors,  $N(\mu, \sigma^2)$  stands for a normal distribution with mean  $\mu$  and variance  $\sigma^2$ ,  $N(\mu, \sigma^2; l, u)$  is a bounded normal distribution with lower and upper limits given by  $l$  and  $u$ , respectively, and  $U(a, b)$  stands for a uniform distribution between  $a$  and  $b$ .

<sup>a</sup> These parameters correspond to the parameterization presented in Espinoza et al. (2019) for sampling physically possible combinations of  $b$  and  $p = R_p/R_*$ . We used an upper and lower allowed value for  $p$  of  $p_l = 0.075$  and  $p_u = 0.125$ , respectively.

<sup>b</sup> Time-averaged equilibrium temperature computed according to Equation (16) of Méndez & Rivera-Valentín (2017).

<sup>c</sup> Transit duration.

implemented in the PyMC3 package through *exoplanet*. We sampled using four chains and 3000 draws, after a tuning run of 4500 draws where the step sizes are optimized. Convergence was verified using the Rubin-Gelman and Geweke statistics. The effective sample size for all parameters, as defined by (Gelman et al. 2013), was  $>4000$ . The priors are detailed in Table 3. Priors for  $M_*$  and  $R_*$  stem from the analysis described in Section 3.1. The priors on  $P$ ,  $T_0$ ,  $\ln(M_p/M_\oplus)$ ,  $e$ , and  $\{a_i\}_{i=0}^1$  were obtained



**Figure 5.** Radial velocities as a function of time for the five spectroscopic instruments used in this work (FEROS, Coralie, CHIRON, NRES, and Minerva). Note that we use a single symbol for Minerva but the observations were made with three different telescopes in the array. The error bars include the posterior values for the jitter terms.

**Table 4**  
Radial Velocities and Bisector Spans for TOI-677<sup>a</sup>

BJD (2,400,000+)	RV <sup>b</sup> (m s <sup>-1</sup> )	$\sigma_{RV}$ (m s <sup>-1</sup> )	BIS (m s <sup>-1</sup> )	$\sigma_{BIS}$ (m s <sup>-1</sup> )	Instrument
58615.051551	-26.62	5.4	...	...	Minerva_T3
58615.051551	-70.76	5.3	...	...	Minerva_T4
58615.072962	-26.25	5.4	...	...	Minerva_T3
58615.072962	-12.28	5.3	...	...	Minerva_T4
58616.005135	-43.36	5.4	...	...	Minerva_T3
58616.026546	-81.33	5.4	...	...	Minerva_T3
58616.047945	-81.42	5.4	...	...	Minerva_T3
58618.484021	-107.13	12.0	34	9	FEROS
58619.499881	-78.23	9.6	47	8	FEROS
58620.482581	-54.73	11.3	14	9	FEROS
58621.616231	42.13	23.5	-51	20	Coralie
58621.623201	-14.62	13.3	...	...	CHIRON
58621.628071	-20.13	13.3	23	10	FEROS
58621.948677	-47.48	5.2	...	...	Minerva_T4
58621.948677	67.59	5.4	...	...	Minerva_T3
58621.970088	-6.47	5.4	...	...	Minerva_T4
58621.970088	-27.69	5.4	...	...	Minerva_T3
58622.467171	-1.33	9.8	35	8	FEROS
58622.623371	14.93	23.1	86	20	Coralie
58622.626601	116.18	24.5	...	...	CHIRON

#### Notes.

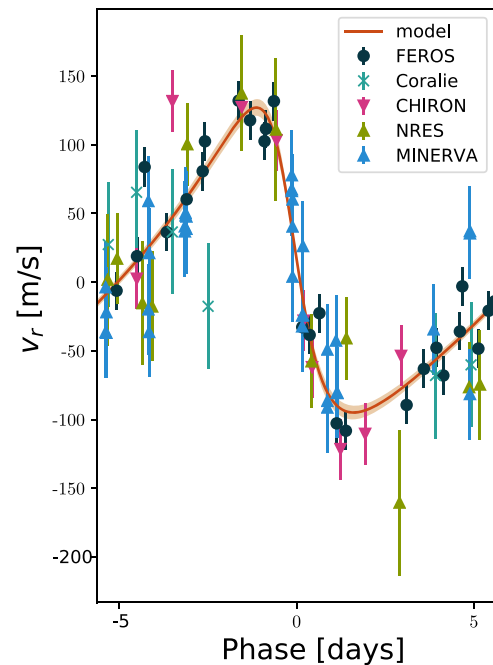
<sup>a</sup> Table 4 is published in its entirety in machine readable format. A portion is shown here for guidance regarding its form and content.

<sup>b</sup> For convenience, the mean has been subtracted from the originally measured radial velocities for each instrument, and the instrument-dependent radial velocity zero-points reported in Table 3 are with respect to these mean-subtracted values. The mean values  $m$  (in m s<sup>-1</sup>) that should be added to recover the original measurements are  $m_{\text{FEROS}} = 37656.23$ ,  $m_{\text{Coralie}} = 37665.27$ ,  $m_{\text{CHIRON}} = 20.1$ ,  $m_{\text{NRES}} = 38228.49$ , and  $m_{\text{Minerva}} = 37844.01$

(This table is available in its entirety in machine-readable form.)

from a fit to the radial velocities alone carried out with the `radvel` package (Fulton et al. 2018).

The posterior model for the radial velocities is shown in Figure 5 as a function of time and in Figure 6 against orbital phase with the quadratic term removed. The posterior model for the photometric observations is shown in Figure 3. Table 3 lists all the priors assumed and the posterior values for the stellar and planetary properties. A fully independent analysis of the data with the `juliet` package (Espinoza et al. 2019) using



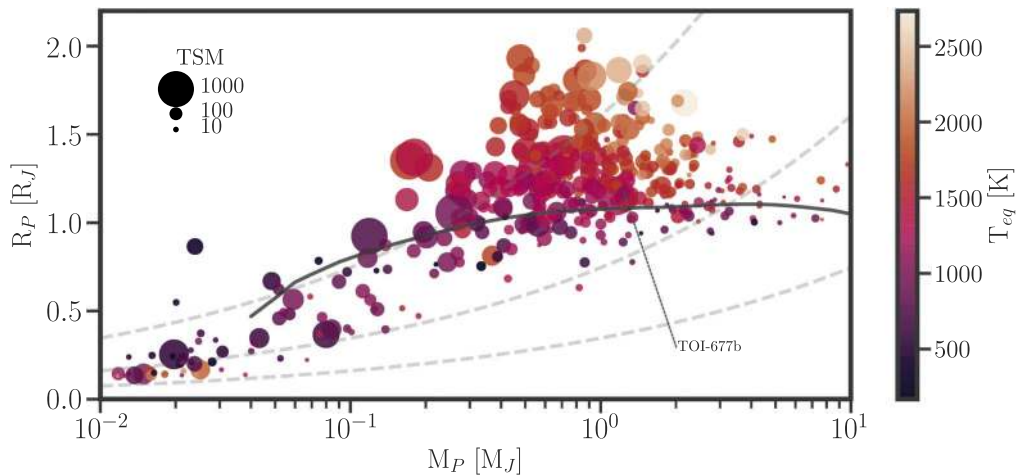
**Figure 6.** Radial velocities as a function of orbital phase for the five spectroscopic instruments used in this work (FEROS, Coralie, CHIRON, NRES, and Minerva). Note that we use a single symbol for Minerva but the observations were made with three different telescopes in the array. The error bars include the posterior values for the jitter terms.

different priors and treatment of photometric and radial velocity trends results in planetary parameters consistent with the ones presented in Table 3. It is noteworthy that besides the Keplerian orbit, there is significant statistical evidence for a long-term trend in the radial velocities, which could be caused by an outer companion. If described by a linear trend the slope is estimated to be  $a_1 = 1.58 \pm 0.19 \text{ m s}^{-1} \text{ day}^{-1}$ .

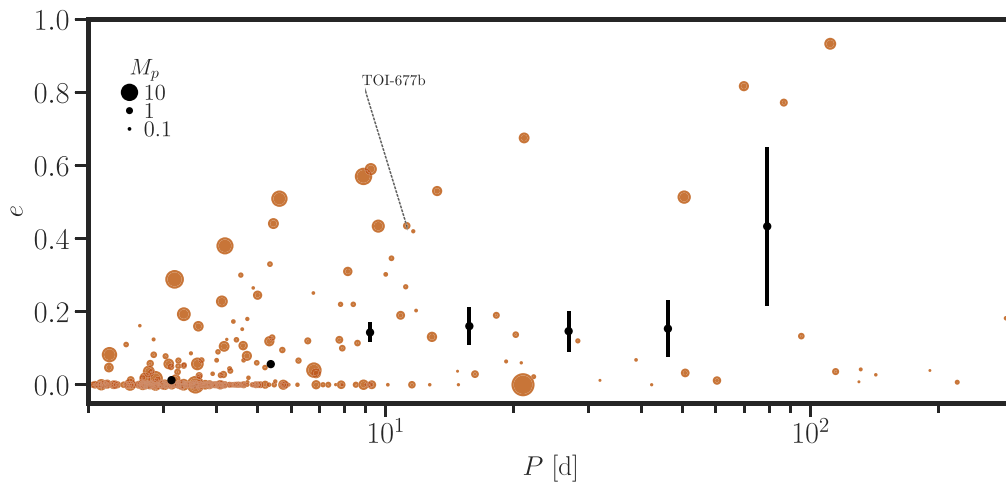
## 4. Discussion

We put TOI-677 b in the context of the population of known, well-characterized<sup>35</sup> transiting exoplanets in Figure 7, where we

<sup>35</sup> We use the catalog of well-characterized planets of Southworth (2011). We restrict the sample to systems whose fractional error on their planetary masses and radii are <25%.



**Figure 7.** Mass–radius diagram for the population of well-characterized transiting planets (Southworth 2011). The point corresponding to TOI-677 b is indicated with a dashed line. The color represents the equilibrium temperature of the planet, while the size scales down with the transmission spectroscopy metric as defined by Kempton et al. (2018). The dashed gray lines correspond to isodensity curves for 0.3, 3, and 30  $\text{g cm}^{-3}$ , respectively. The solid line corresponds to the predicted radius using the models of Fortney et al. (2007) for a planet with a  $10 M_{\oplus}$  central core.



**Figure 8.** Period–eccentricity diagram for the population of well characterized transiting planets. The point corresponding to TOI-677 b is indicated with a dashed line. The size scales with the mass of the planet. The black points with error bars are the average eccentricities of the sample in bins that are equally spaced in  $\log(P)$  for  $P < 100$  days.

show a scatter plot of planetary mass versus planetary radius, coding with color the equilibrium temperature. The orbit averaged incident flux for TOI-677 b is  $\approx 3.9 \times 10^8 \text{ erg s}^{-1} \text{ cm}^{-2}$ , close to the value of  $\approx 2 \times 10^8 \text{ erg s}^{-1} \text{ cm}^{-2}$  below which it has been shown that the effects of irradiation on the planetary radius are negligible (e.g., Demory & Seager 2011). The radius of TOI-677 b is in line with what is expected for a gas giant with a core of  $M_C = 10 M_{\oplus}$  according to the standard models of Fortney et al. (2007). This underscores the value of warm giants, whose structure can be modeled without the complications of an incident flux resulting in radius inflation (Kovács et al. 2010; Demory & Seager 2011). Figure 7 also shows that TOI-677 b, having a transmission spectroscopy metric (Kempton et al. 2018) of  $\approx 100$ , is not a particularly well-suited target of transmission spectroscopy studies, if compared with the rest of the population of close-in giant planets.

In Figure 8 we plot the same population of well-characterized planets in the period–eccentricity plane, coding the planetary mass with the symbol size. It is apparent that TOI-677 b lies in a part of this plane that is still sparsely

populated. The eccentricity of exoplanets is very low for close-in systems, and starts to grow for periods of  $P \gtrsim 4$  days. With an eccentricity of  $e = 0.435 \pm 0.024$ , TOI-677 b lies in the upper range of eccentricity values for planets with similar periods in the currently known sample. Besides the significant eccentricity of the orbit of TOI-677 b, the presence of a long-term trend in the radial velocities is interesting in the context of migration mechanisms of giant planets. Warm Jupiters can be formed via secular gravitational interactions with an outer planet followed by tidal interactions with the star in the high eccentricity stage of the secular cycle (e.g., Kozai 1962). In this context, Dong et al. (2014) predict that in order to overcome the precession caused by general relativity, the warm Jupiters produced via this mechanism should have outer planets at relatively short orbital distances that can be detected with a radial velocity monitoring. At the moment we cannot provide meaningful constraints on a potential outer companion. We will continue to monitor the system with radial velocities to determine the exact nature of the long-term radial velocity we uncovered.





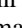


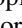
The determination of the orbital obliquity of transiting planets through the Rossiter–McLaughlin (R–M) effect, particularly for planets with orbital periods longer than  $\approx 10$  days, provides a powerful tool to constrain migration theories (Petrovich & Tremaine 2016). With a sizable  $v \sin i$  of  $7.80 \pm 0.19 \text{ km s}^{-1}$  and a bright magnitude of  $V = 9.8$  mag, TOI-677 b is a prime target to perform a measurement of the projected angle between the stellar and orbital angular momenta. Specifically, the expected semi-amplitude of the R–M signal for TOI-677 b in the case of an aligned orbit is of  $K_{R-M} = 70 \pm 10 \text{ m s}^{-1}$ . While still based on a very limited population, the current obliquity distribution of transiting planets with similar periods as TOI-677 b seems to follow a similar behavior to that of the eccentricity distribution, with a large spread in their values. Current discoveries include aligned systems like WASP-84b (Anderson et al. 2015) and HAT-P-17b (Fulton et al. 2013), mildly misaligned systems (WASP-8b; Queloz et al. 2010). The measurement of the obliquity of TOI-677 b will increment this small sample and help in further understanding how close-in giant planets form.

A.J. acknowledges support from FONDECYT project 1171208 and by the Ministry for the Economy, Development, and Tourism’s Programa Iniciativa Científica Milenio through grant IC 120009, awarded to the Millennium Institute of Astrophysics (MAS). R.B. acknowledges support from FONDECYT Postdoctoral Fellowship Project 3180246, and from the Millennium Institute of Astrophysics (MAS). M.B. acknowledges CONICYT-GEMINI grant 32180014. T.D. acknowledges support from MIT’s Kavli Institute as a Kavli postdoctoral fellow. Resources supporting this work were provided by the NASA High-End Computing (HEC) Program through the NASA Advanced Supercomputing (NAS) Division at Ames Research Center for the production of the SPOC data products. This work has made use of data from the European Space Agency (ESA) mission *Gaia* (<https://www.cosmos.esa.int/gaia>), processed by the *Gaia* Data Processing and Analysis Consortium (DPAC, <https://www.cosmos.esa.int/web/gaia/dpac/consortium>). Funding for the DPAC has been provided by national institutions, in particular the institutions participating in the *Gaia* Multilateral Agreement. This research made use of exoplanet (Foreman-Mackey et al. 2019) and its dependencies (Astropy Collaboration et al. 2013, 2018; Kipping 2013; Salviatier et al. 2016; Theano Development Team 2016; Espinoza 2018; Foreman-Mackey et al. 2019; Luger et al. 2019). Minerva-Australis is supported by Australian Research Council LIEF grant LE160100001, Discovery grant DP180100972, Mount Cuba Astronomical Foundation, and institutional partners University of Southern Queensland, UNSW Australia, MIT, Nanjing University, George Mason University, University of Louisville, University of California Riverside, University of Florida, and The University of Texas at Austin. We respectfully acknowledge the traditional custodians of all lands throughout Australia, and recognise their continued cultural and spiritual connection to the land, waterways, cosmos, and community. We pay our deepest respects to all elders, ancestors, and descendants of the Giabal, Jarowair, and Kambuwal nations, upon whose lands the Minerva-Australis facility at Mt. Kent is situated.

*Facilities:* TESS, FEROS/MPG2.2 m, Coralie/Euler1.3 m, NRES/LCOGT1m, Shared Skies Telescope/Mount Kent Observatory, CTIO 1.5 m/CHIRON.

*Software:* CERES (Brahm et al. 2017a; Jordán et al. 2014), ZASPE (Brahm et al. 2017b, 2015), radvel (Fulton et al. 2018), exoplanet (Foreman-Mackey et al. 2019), juliet (Espinoza et al. 2019).

## ORCID iDs

Andrés Jordán  <https://orcid.org/0000-0002-5389-3944>  
 Rafael Brahm  <https://orcid.org/0000-0002-9158-7315>  
 Néstor Espinoza  <https://orcid.org/0000-0001-9513-1449>  
 Paula Sarkis  <https://orcid.org/0000-0001-8128-3126>  
 Trifon Trifonov  <https://orcid.org/0000-0002-0236-775X>  
 Mauro Barbieri  <https://orcid.org/0000-0001-8362-3462>  
 Allen Davis  <https://orcid.org/0000-0002-5070-8395>  
 Daniel Bayliss  <https://orcid.org/0000-0001-6023-1335>  
 Luke Bouma  <https://orcid.org/0000-0002-0514-5538>  
 Diana Dragomir  <https://orcid.org/0000-0003-2313-467X>  
 Jason D. Eastman  <https://orcid.org/0000-0003-3773-5142>  
 Tansu Daylan  <https://orcid.org/0000-0002-6939-9211>  
 Natalia Guerrero  <https://orcid.org/0000-0002-5169-9427>  
 Thomas Barclay  <https://orcid.org/0000-0001-7139-2724>  
 Roland Vanderspek  <https://orcid.org/0000-0001-6763-6562>  
 David W. Latham  <https://orcid.org/0000-0001-9911-7388>  
 Joshua Winn  <https://orcid.org/0000-0002-4265-047X>  
 Jon M. Jenkins  <https://orcid.org/0000-0002-4715-9460>  
 Robert A. Wittenmyer  <https://orcid.org/0000-0001-9957-9304>  
 Brendan P. Bowler  <https://orcid.org/0000-0003-2649-2288>  
 Jonathan Horner  <https://orcid.org/0000-0002-1160-7970>  
 Stephen R. Kane  <https://orcid.org/0000-0002-7084-0529>  
 John F. Kielkopf  <https://orcid.org/0000-0003-0497-2651>  
 Timothy D. Morton  <https://orcid.org/0000-0002-8537-5711>  
 Peter Plavchan  <https://orcid.org/0000-0002-8864-1667>  
 C. G. Tinney  <https://orcid.org/0000-0002-7595-0970>  
 Markus Rabus  <https://orcid.org/0000-0003-2935-7196>  
 Avi Shporer  <https://orcid.org/0000-0002-1836-3120>  
 Carl Ziegler  <https://orcid.org/0000-0002-0619-7639>  
 Andrew W. Mann  <https://orcid.org/0000-0003-3654-1602>

## References

- Addison, B., Wright, D. J., Wittenmyer, R. A., et al. 2019, *PASP*, 131, 115003  
 Albrecht, S., Winn, J. N., Johnson, J. A., et al. 2012, *ApJ*, 757, 18  
 Anderson, D. R., Triana, A. H. M. J., Turner, O. D., et al. 2015, *ApJL*, 800, L9  
 Anglada-Escudé, G., & Butler, R. P. 2012, *ApJS*, 200, 15  
 Astropy Collaboration, Price-Whelan, A. M., Sipőcz, B. M., et al. 2018, *AJ*, 156, 123  
 Astropy Collaboration, Robitaille, T. P., Tollerud, E. J., et al. 2013, *A&A*, 558, A33  
 Bakos, G., Noyes, R. W., Kovács, G., et al. 2004, *PASP*, 116, 266  
 Bakos, G. Á., Csabry, Z., Penev, K., et al. 2013, *PASP*, 125, 154  
 Barclay, T., Pepper, J., & Quintana, E. V. 2018, *ApJS*, 239, 2  
 Borucki, W. J., Koch, D., Basri, G., et al. 2010, *Sci*, 327, 977  
 Brahm, R., Espinoza, N., Jordán, A., et al. 2019, *AJ*, 158, 45  
 Brahm, R., Jordán, A., Bakos, G. Á., et al. 2016, *AJ*, 151, 89  
 Brahm, R., Jordán, A., & Espinoza, N. 2017a, *PASP*, 129, 034002  
 Brahm, R., Jordán, A., Hartman, J., & Bakos, G. 2017b, *MNRAS*, 467, 971  
 Brahm, R., Jordán, A., Hartman, J. D., et al. 2015, *AJ*, 150, 33  
 Cardelli, J. A., Clayton, G. C., & Mathis, J. S. 1989, *ApJ*, 345, 245  
 Castelli, F., & Kurucz, R. L. 2004, arXiv:astro-ph/0405087  
 Dawson, R. I. 2014, *ApJL*, 790, L31  
 Dawson, R. I., & Johnson, J. A. 2018, *ARA&A*, 56, 175  
 Demory, B.-O., & Seager, S. 2011, *ApJS*, 197, 12  
 Dong, S., Katz, B., & Socrates, A. 2014, *ApJL*, 781, L5  
 Engel, M., Shahaf, S., & Mazeh, T. 2017, *PASP*, 129, 065002  
 Espinoza, N. 2018, *RNAAS*, 2, 209  
 Espinoza, N., & Jordán, A. 2015, *MNRAS*, 450, 1879  
 Espinoza, N., Kossakowski, D., & Brahm, R. 2019, *MNRAS*, 490, 2262

- Foreman-Mackey, D., Czekala, I., Agol, E., et al. 2019, *dfm/exoplanet: exoplanet v0.2.0*, doi:[10.5281/zenodo.3359880](https://doi.org/10.5281/zenodo.3359880)
- Foreman-Mackey, D., Hogg, D. W., Lang, D., & Goodman, J. 2013, *PASP*, **125**, 306
- Fortney, J. J., Marley, M. S., & Barnes, J. W. 2007, *ApJ*, **659**, 1661
- Fulton, B. J., Howard, A. W., Winn, J. N., et al. 2013, *ApJ*, **772**, 80
- Fulton, B. J., Petigura, E. A., Blunt, S., & Sinukoff, E. 2018, *PASP*, **130**, 044504
- Gaia Collaboration, Brown, A. G. A., Vallenari, A., et al. 2018, *A&A*, **616**, A1
- Gaia Collaboration, Prusti, T., de Bruijne, J. H. J., et al. 2016, *A&A*, **595**, A1
- Gelman, A., Carlin, J., Stern, H., et al. 2013, *Bayesian Data Analysis* (3rd Ed.; Boca Raton, FL: CRC Press)
- Hoffman, M., & Gelman, A. 2011, *JMLR*, **15**, 1593
- Huber, D., Chaplin, W. J., Chontos, A., et al. 2019, *AJ*, **157**, 245
- Husser, T. O., Wende-von Berg, S., Dreizler, S., et al. 2013, *A&A*, **553**, A6
- Jenkins, J. M., Twicken, J. D., McCauliff, S., et al. 2016, *Proc. SPIE*, **9913**, 99133E
- Jones, M. I., Brahm, R., Espinoza, N., et al. 2019, *A&A*, **625**, A16
- Jordán, A., Brahm, R., Bakos, G. Á, et al. 2014, *AJ*, **148**, 29
- Kaufer, A., Stahl, O., Tubbesing, S., et al. 1999, *Msngr*, **95**, 8
- Kempton, E. M.-R., Bean, J. L., Louie, D. R., et al. 2018, *PASP*, **130**, 114401
- Kipping, D. M. 2013, *MNRAS*, **435**, 2152
- Kovács, G., Bakos, G. Á, Hartman, J. D., et al. 2010, *ApJ*, **724**, 866
- Kozai, Y. 1962, *AJ*, **67**, 591
- Lendl, M., Triaud, A. H. M. J., Anderson, D. R., et al. 2014, *A&A*, **568**, A81
- Li, G., & Winn, J. N. 2016, *ApJ*, **818**, 5
- Li, J., Tenenbaum, P., Twicken, J. D., et al. 2019, *PASP*, **131**, 024506
- Luger, R., Agol, E., Foreman-Mackey, D., et al. 2019, *AJ*, **157**, 64
- Mayor, M., Pepe, F., Queloz, D., et al. 2003, *Msngr*, **114**, 20
- Méndez, A., & Rivera-Valentín, E. G. 2017, *ApJL*, **837**, L1
- Miller, N., & Fortney, J. J. 2011, *ApJL*, **736**, L29
- Pepper, J., Pogge, R. W., DePoy, D. L., et al. 2007, *PASP*, **119**, 923
- Petrovich, C., & Tremaine, S. 2016, *ApJ*, **829**, 132
- Pollacco, D. L., Skillen, I., Collier Cameron, A., et al. 2006, *PASP*, **118**, 1407
- Queloz, D., Anderson, D. R., Collier Cameron, A., et al. 2010, *A&A*, **517**, L1
- Ricker, G. R., Winn, J. N., Vanderspek, R., et al. 2015, *JATIS*, **1**, 014003
- Rodriguez, J. E., Quinn, S. N., Huang, C. X., et al. 2019, *AJ*, **157**, 191
- Salvatier, J., Wiecki, T. V., & Fonnesbeck, C. 2016, *PeerJ Computer Science*, **2**, e55
- Siverd, R. J., Brown, T. M., Barnes, S., et al. 2018, *Proc. SPIE*, **10702**, 107026C
- Smith, J. C., Stumpe, M. C., Van Cleve, J. E., et al. 2012, *PASP*, **124**, 1000
- Southworth, J. 2011, *MNRAS*, **417**, 2166
- Stassun, K. G., & Torres, G. 2018, *ApJ*, **862**, 61
- Stumpe, M. C., Smith, J. C., Catanzarite, J. H., et al. 2014, *PASP*, **126**, 100
- Sullivan, P. W., Winn, J. N., Berta-Thompson, Z. K., et al. 2015, *ApJ*, **809**, 77
- Talens, G. J. J., Albrecht, S., Spronck, J. F. P., et al. 2017, *A&A*, **606**, A73
- Theano Development Team 2016, arXiv:1605.02688
- Tokovinin, A. 2018, *PASP*, **130**, 035002
- Tokovinin, A., Fischer, D. A., Bonati, M., et al. 2013, *PASP*, **125**, 1336
- Twicken, J. D., Catanzarite, J. H., Clarke, B. D., et al. 2018, *PASP*, **130**, 064502
- Wang, S., Jones, M., Shporer, A., et al. 2019, *AJ*, **157**, 51
- Welch, P. D. 1967, *IEEE Trans. Audio & Electroacoust.*, **15**, 70
- Ziegler, C., Tokovinin, A., Briceno, C., et al. 2020, *AJ*, **159**, 19